Article

Synthesis and Characterization of Indium-Doped SnO$_2$-Based Impedance Spectroscopy Sensor for Real-Time Humidity Sensing Applications

Birhanu Alemayehu [1], Eunsung Shin [1], Vladimir Vasilyev [2] and Guru Subramanyam [1,*]

[1] Center of Excellence for Thin-Film Research and Surface Engineering, Department of Electrical and Computer Engineering, University of Dayton, Dayton, OH 45469, USA; alemayehub2@udayton.edu (B.A.); eshin1@udayton.edu (E.S.)

[2] Air Force Research Laboratory, Sensors Directorate, Wright Patterson AFB, Fairborn, OH 45433, USA; vladimir.vasilyev.1@us.af.mil

* Correspondence: gsubramanyam1@udayton.edu

Abstract: Metallic transition-metal dichalcogenides are emerging as promising electrode materials for applications such as 2D electronic devices owing to their good electrical conductivity. In this study, a high-performance humidity sensor based on NbTe$_2$ electrode material and an indium-doped SnO$_2$ thin film sensing layer was fabricated using a pulsed laser deposition system. The morphology, structural, elemental compositions, and electrical properties of the as-deposited samples were characterized. Additionally, the humidity sensing response of the fabricated sensor with In-doped SnO$_2$ (8:92 wt%) sensing film was evaluated in a wide range of relative humidity at room temperature. The results demonstrated that the humidity sensor based on In-doped SnO$_2$ exhibited a high sensitivity of 103.1 Ω/%RH, fast response and recovery times, a low hysteresis value, good linearity, and repeatability. In addition, the sensor had good long-term stability, with a variation in impedance of less than 3%. The results indicated that the humidity sensor could be suitable for practical humidity sensing applications.

Keywords: humidity sensor; In-doped SnO$_2$; pulsed laser deposition; inter-digitated transducer; NbTe$_2$ electrode

1. Introduction

Since the discovery of graphene [1], the family of two-dimensional (2D) atomically thin materials has recently attracted considerable research interest, offering exciting potential in the fields of nanoelectronics, optoelectronics, and photovoltaics [2–6]. Among 2D materials, transition metal dichalcogenides (TMDs), formulated as MX$_2$ (M = transition metal (e.g., Mo, W, etc.) and X = chalcogen (S, Se, and Te)), have gained a lot of attention due to their unique structures, such as good flexibility, and novel physical or chemical properties [7–10]. Depending on the variation in the band structure, TMDs can be semiconducting TMDs or metallic TMDs (MTMDs) [11]. According to [12–16], MTMDs exhibited various fascinating physical phenomena, such as ferromagnetism, charge density waves, and superconductivity. In particular, conductive MTMD materials have been used in multiple fields of applications, such as energy storage and electronic devices [17,18]. For example, vanadium dichalcogenides were used as electrode materials to manufacture sensors, supercapacitors, and lithium-ion batteries [19–21]. MTMDs generally have high electrical conductivity comparable to that of conventional metals, making them excellent electrode materials for the fabrication of electronic devices. In this context, the metal tellurides of the VB group (VTe$_2$, NbTe$_2$, and TaTe$_2$) offer significant potential in applications requiring good electrical conductivity and structural advantages such as flexibility and conformal electrodes for wearable sensors.

Exploring the aforementioned physical properties and versatile applications requires the controlled synthesis of MTMD materials with different thicknesses, large-area films/nanosheets, and high-crystalline structures. To date, numerous techniques have been applied to synthesize 2D materials. For instance, liquid-based and mechanical exfoliations have been widely used to synthesize a few layers of 2D materials due to their simplicity [22,23]. However, these techniques have some drawbacks, such as the multiple steps involved in synthesis, contamination, and the difficulty of precisely controlling the thickness and size of nanosheets [24,25]. Alternatively, chemical vapor deposition (CVD) has been proven to be one of the most effective techniques for synthesizing a wide range of highly scalable TMD nanosheets [1,26–29]. It is well known that the CVD process is typically performed at high temperatures, which instantly crystallizes the film. Normally, photolithography is used to pattern the crystallized film or fabricate electronic devices.

However, the development of an adequate photolithography process for 2D materials is still in its early stages [30]. This circumstance limits the widespread use of the CVD technique in the fabrication of electrical devices based on MTMD material [31,32]. Therefore, the controllable synthesis of MTMD materials with a reduced deposition temperature has become a hot topic. Pulsed laser deposition (PLD) is an impressive alternative to the above techniques due to its unique advantages, such as easily controllable deposition parameters, high scalability, room-temperature deposition, precise stoichiometry, and control of film thickness and size [33–35]. Grangeon et al. reported controllable growth of thin films of niobium telluride ($NbTe_2$) at elevated deposition temperatures using the PLD technique. They demonstrated the effect of adjusting the deposition parameters on the formation of the different phases of $NbTe_2$ [36]. However, after that, reports on how to synthesize $NbTe_2$ using PLD were unexpectedly absent for a long time. Here, we report a controllable synthesis of a thin film of $NbTe_2$ using PLD at room temperature, as well as the application of the fabricated film as an electrode in the form of an interdigitated transducer (IDT) in the development of an impedance spectroscopy-type humidity sensor.

Monitoring the humidity level in the surrounding environment has become a major concern in many sectors, such as manufacturing industries, health care centers, homes, the environment, and agriculture [37]. An excellent humidity sensor must meet several criteria, including fast response time, short recovery time, high sensitivity, good reproducibility, and long-term stability [38,39]. Several sensing materials/films, such as carbon-based materials, conductive polymers, and semiconducting materials, have been used to develop humidity sensors. Among these, metal oxide semiconductors, including zinc oxide (ZnO), iron (III) oxide (Fe_2O_3), tin oxide (SnO_2), nickel oxide (NiO), and titanium oxide (TiO_2), have continued to be the focus of significant attention in the planning and development of highly sensitive humidity sensors [40–44]. Specifically, SnO_2 is the most promising candidate for humidity sensors due to its fascinating chemical and physical properties, such as chemical sensitivity to oxygen and water vapor, high chemical stability, non-toxicity, and low cost [45]. SnO_2 is an n-type semiconductor with a wider band gap. However, the pristine SnO_2 humidity sensors exhibited insufficient response, poor linearity, and long response and recovery times [46,47]. Thus, several effective strategies have been implemented to improve the sensing performance of SnO_2-based sensors. For example, doping of sensing materials with other metal oxides or metal ions is predominant, resulting in increased surface areas/active sites and heterogeneous interfaces between the host and the dopant that facilitate an effective water adsorption/desorption process [48–50].

In this study, we present the synthesis of an indium (In)-doped SnO_2 sensing film using the PLD technique and investigate its application for humidity sensing at room temperature. The effect of the different weight percentages of In in SnO_2 was investigated [51–54]. To our knowledge, the use of In-doped SnO_2 film for humidity sensing applications at room temperature has not yet been reported. An impedance spectroscopy-based humidity sensor was fabricated by depositing the sensing film on the interdigitated transducer. The crystalline structure, morphology, chemical composition, and electrical characteristics of the In-doped SnO_2 and $NbTe_2$ films were examined with X-ray diffraction (XRD), scanning

electron microscopy (SEM), energy dispersive spectroscopy (EDS), and a four-point probe sheet resistance measurement method. The humidity sensing performance of the fabricated impedance spectroscopy-based sensor was evaluated over a wide range of relative humidity (RH) with a simple test setup. The sensor based on In-doped SnO_2 exhibited high sensitivity, good linearity, fast response and recovery times, and low hysteresis. In-doped SnO_2 has good potential for health monitoring and environmental detection, given its humidity-sensing capability.

2. Materials and Methods

### 2.1. Materials

In-doped SnO_2 (SnO_2 92/In 8 wt%) and $NbTe_2$ ceramic targets were purchased from Kurt J. Lesker Co., Jefferson Hills, PA, USA, and high-resistivity silicon substrates were obtained from University Wafer Inc., South Boston, MA, USA. All chemicals were ensured to be analytical grade, applied directly without further purification, and distilled water was used in the experiments.

2.2. Methods

2.2.1. Interdigitated Transducer Fabrication Process

A standard positive photoresist lift-off process with S1813 photoresist was used to pattern the $NbTe_2$ film to fabricate the interdigitated transducer (IDT) structure. The thin film of $NbTe_2$ was deposited onto the pattered wafer at room temperature using a KrF excimer laser (λ = 248 nm) to ablate the $NbTe_2$ target [55]. After the lift-off process, the wafer was annealed in a conventional furnace to crystallize the film. Thin films of 20 nm Ti and 330 nm Au were deposited using e-beam evaporation as contacts using another lift-off lithography process. Figure 1 illustrates the main process for fabricating the humidity sensor based on the metallic $NbTe_2$ film. IDTs were used to measure the impedance changes of In-doped SnO_2 during exposure to various levels of relative humidity.
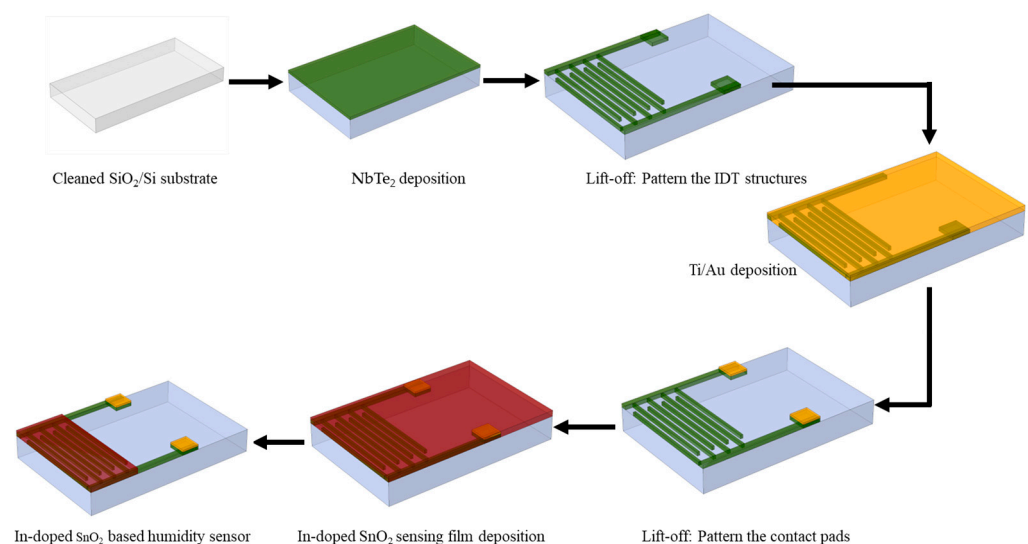

Figure 1. Schematic showing the main fabrication process for the In-doped SnO_2 thin film-based humidity sensor with the $NbTe_2$ electrode.

2.2.2. Sensing Film Fabrication

The sensing film, a 100 nm thick sensing In-doped SnO_2 film, was also deposited using a positive photoresist lithography process on top of the $NbTe_2$ IDT structures. The In-doped SnO_2 target (SnO_2 92/In 8 wt%) was used for the synthesis of In-doped SnO_2 thin films [55] using a 248 nm KrF excimer laser. 600 laser pulses were used to obtain a 100 nm film. After the lift-off process, the wafer was annealed in a furnace at 330 °C to crystallize the In-doped SnO_2 film. The wafer was diced and then cleaned. Figure 2 shows

the microscopic picture of the NbTe$_2$-based fabricated impedance-type sensor with the In-doped SnO$_2$ sensing film. The width of the finger and the spacing between the fingers were 160 and 80 μm, respectively.
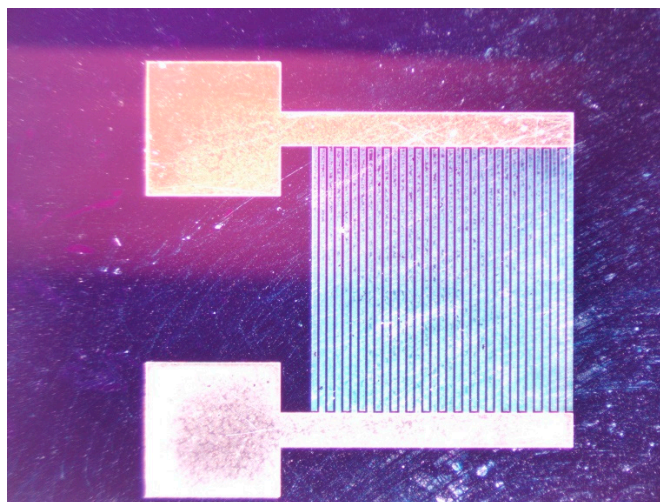
Figure 2. A microscopic picture of a fabricated impedimetric humidity sensor.

2.2.3. Characterization

The crystal structure of the NbTe$_2$ and In-doped SnO$_2$ samples was carried out on a PANalytical X-Pert diffractometer with a hybrid monochromator for Cu Kα_1 radiation (λ = 1.554056 Å). The diffraction patterns were collected at a scan angle (2θ) ranging from 8 to 90° with a step size of 0.02°. The morphology, structure, and elemental composition of the NbTe$_2$ and In-doped SnO$_2$ samples were studied using a high-resolution scanning electron microscope (HRSEM, Hitachi S-4800, Hitachi, Japan) at an acceleration voltage of 10 kV and energy-dispersive spectroscopy (EDS, Zeiss EVO-50XVP, Jena, Germany) instruments. The surface electrical conductivity of the prepared thin film samples was measured using the four-point probe sheet resistance tester (Ossila).

2.2.4. Humidity Sensing

The humidity sensing of the fabricated sensor was evaluated at room temperature using a custom-made experimental setup for the measurement of relative humidity, where the sensor was enclosed in a test chamber to maintain consistent sensing conditions, as shown in Figure 3. The sensor was then connected to a handheld impedance analyzer (AD5940, Analog Devices, Wilmington, MA, USA) to measure the impedance response of the sensor at different RH levels. For data logging, the impedance analyzer was connected directly to the PC. Additionally, a commercially available humidity sensor (HTU21D, humidity precision: 2% RH, humidity resolution: 0.1% RH, SparkFun Electronics, Boulder, CO, USA), which serves as a reference, was placed side by side with the fabricated sensors to measure the relative humidity level within the test chamber. Analog data from this device was logged onto the PC through an Arduino microcontroller. The system also included a mass flow controller (GA50A, MKS, Andover, MA, USA) and a humidifier. Initially, nitrogen gas (N$_2$) was introduced into the test chamber to purge the entire test setup and establish a baseline. The humid air or moisture was generated by the humidifier. Different levels of RH were achieved by adjusting the flow rate of N$_2$ through the mass flow controller and mixing it with humid air in the mixer. Then, the impedance changes of the In-doped SnO$_2$ film were measured during cyclic exposure to nitrogen and moist air using the impedance analyzer. Sensor impedance values were measured at an operating frequency of 35 kHz due to the improved sensitivity of the device between 30 and 40 kHz [55].
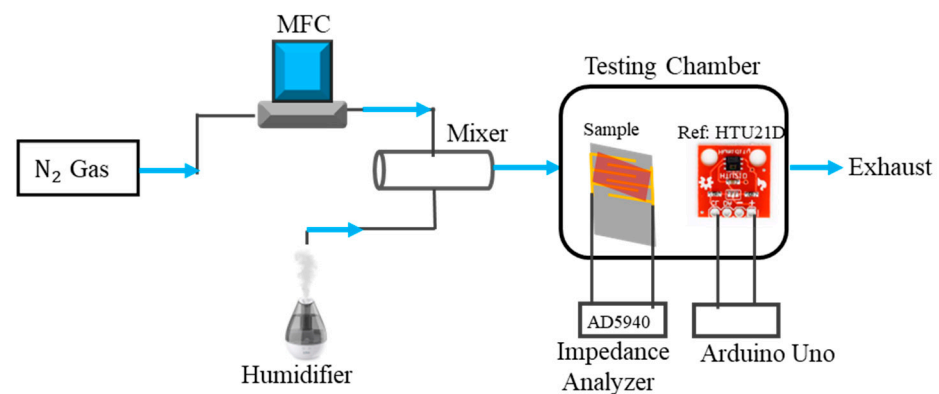
Figure 3. Block diagram of the experimental setup for humidity sensing.

3. Results

3.1. Film Characterization

Before fabricating the $NbTe_2$-based humidity sensor, a preliminary investigation was performed to determine the optimal PLD deposition parameters and the annealing temperature to grow thin films of both $NbTe_2$ and In-doped SnO_2. Once these parameters were identified, a thin film of $NbTe_2$ was deposited onto a silicon substrate, and the crystal structure of the sample was analyzed using XRD. Figure 4 shows the XRD pattern obtained for the as-deposited $NbTe_2$ sample. As can be seen in the figure, the diffraction peaks of the sample were sharp and strong in intensity, indicating complete crystallization of $NbTe_2$. Moreover, the XRD peaks were well-matched with those of the monoclinic crystal structure of $NbTe_2$. For example, the 2θ diffraction peaks of the sample at $\sim 13.1°$, $26.4°$, $40°$, and $54.4°$ were indexed to the (0 0 1), (0 0 2), (3 1 1), and (-7 1 5) planes of $NbTe_2$ (JCPDS No. 21-0605). Furthermore, the absence of other diffraction peaks confirmed the sample's phase purity.
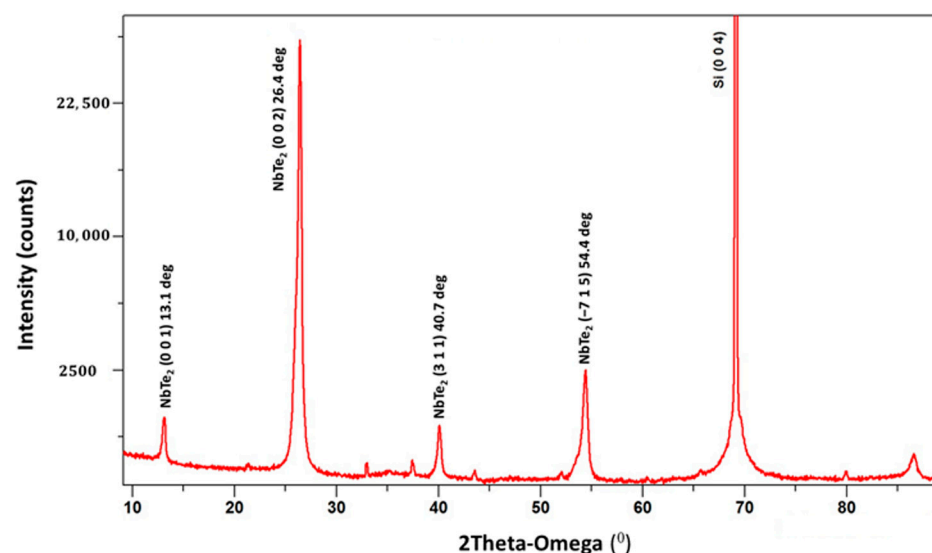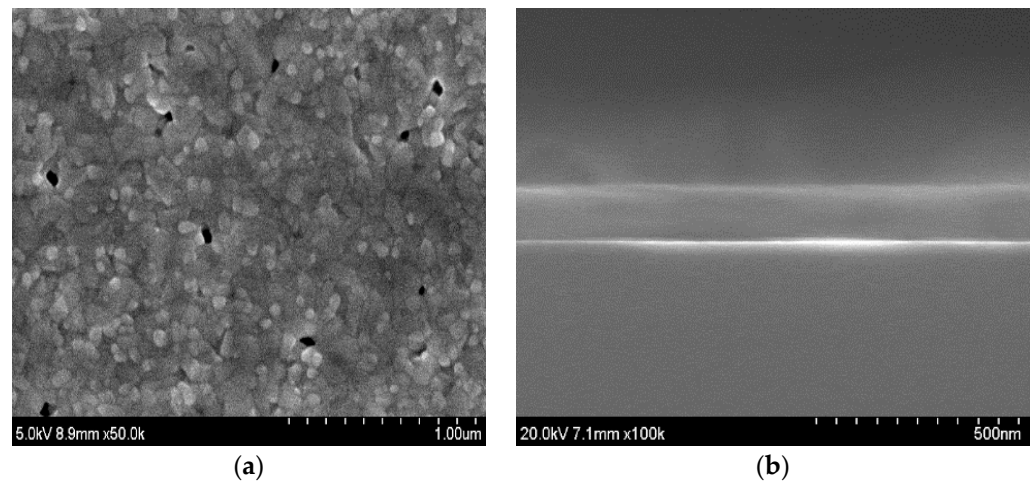

Figure 4. XRD pattern of the $NbTe_2$ film deposited using PLD. XRD peaks represent the crystalline phase of $NbTe_2$ (the monoclinic crystal structure).
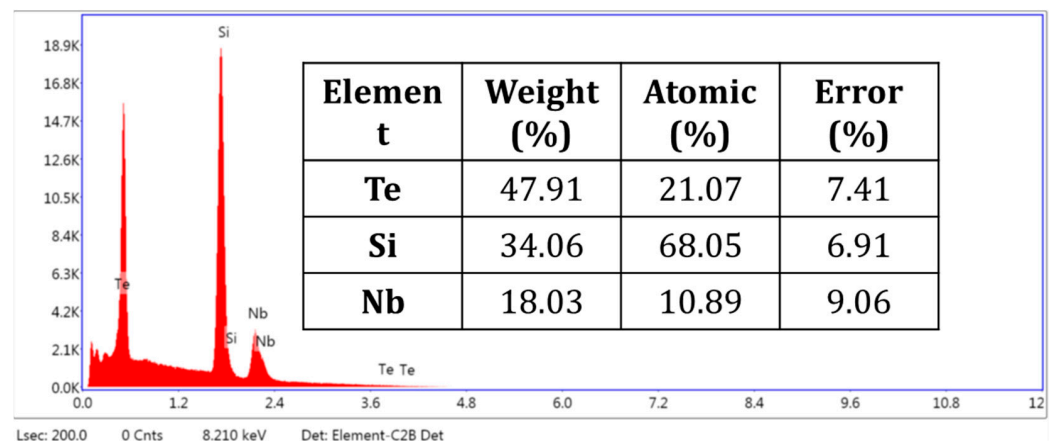
Figure 5 shows the SEM images of the surface of the $NbTe_2$ film deposited onto the silicon substrate. As can be seen in Figure 5a, a thin film of $NbTe_2$ with no known defects was grown using PLD. The cross-sectional view (Figure 5b) reveals that the film had a dense and integrated structure with good adhesion that can reflect the quality of the film. In addition, the formation of nanopores was observed. The EDS spectrum of the as-deposited $NbTe_2$ film grown on the silicon substrate (Figure 6) contains the peaks of niobium and tellurium. From the percentage of atomic weight, the atomic ratio of Te to Nb was calculated

and found to be 1.94, which was very close to the theoretical value of $NbTe_2$, suggesting that the sample was stoichiometric $NbTe_2$. The electrical conductivity of $NbTe_2$ was measured and found to be ~28.4 S/m.


(**a**)   (**b**)

Figure 5. SEM images of the $NbTe_2$ film: (**a**) top view; (**b**) cross-sectional view.

| Element	Weight (%)	Atomic (%)	Error (%)
Te	47.91	21.07	7.41
Si	34.06	68.05	6.91
Nb	18.03	10.89	9.06

Figure 6. EDS spectrum profile of the as-grown $NbTe_2$ film.

Similarly, the crystalline structure, morphology, and elemental composition of In-doped SnO_2 were studied. A thin film of In-doped SnO_2 (8:92 wt%) was deposited onto the silicon substrate and crystallized in the furnace. Figure 7 shows the XRD pattern of the In-doped SnO_2 film. The diffraction peaks of In-doped SnO_2 at 2θ of 26.58°, 33.86°, and 51.76° were indexed to the (1 1 0), (0 1 1), and (1 2 1) planes of the tetragonal cassiterite phase of SnO_2 (JCPDS No: 41-1445). Moreover, it is clear that In was incorporated into the SnO_2 lattice because no other secondary phases, such as In or In_2O_3, were observed.
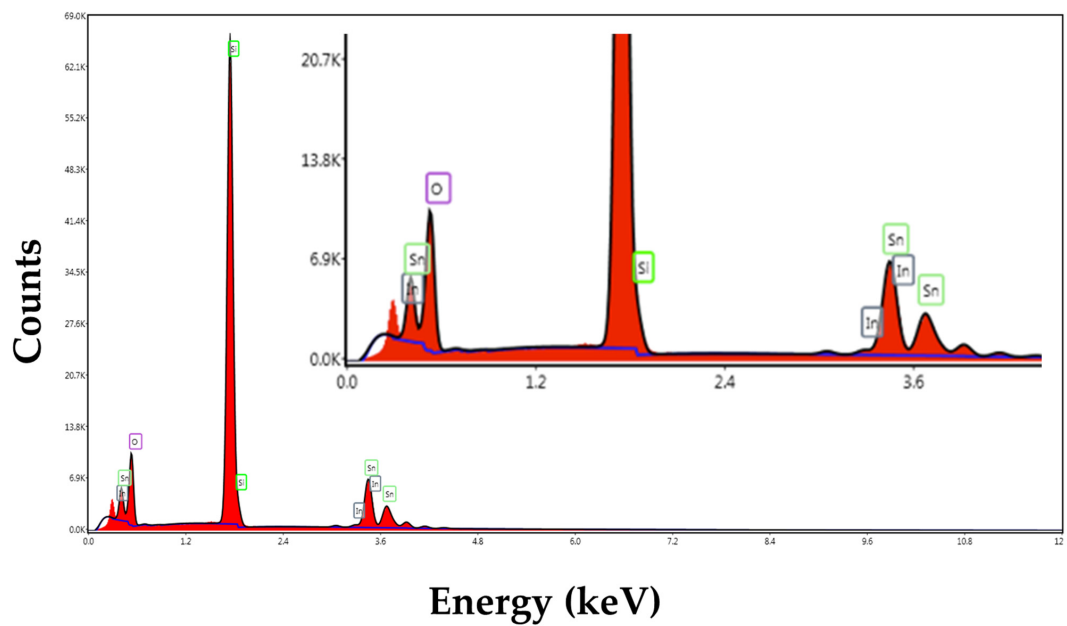
The SEM image of the as-deposited In-doped SnO_2 sample presented in Figure 8 shows that a uniform and smooth surface was obtained. Also, no known defects were observed on the surface of the film. The analysis of the EDS spectrum of the In-doped SnO_2 film presented in Figure 9 confirmed the existence of In, Sn, and O elements in the deposited thin film. Furthermore, the elementary mappings demonstrated that all elements, such as In, Sn, and O, were uniformly distributed on the film's surface.
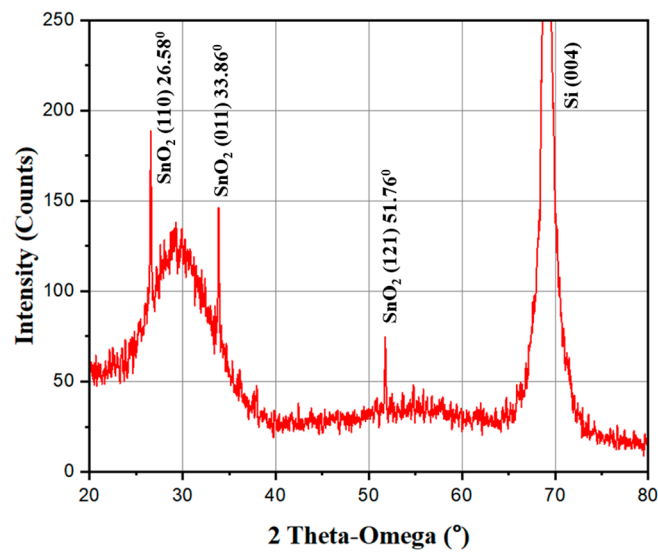
Figure 7. XRD spectroscopy of the In-doped SnO_2 film deposited using PLD. XRD peaks represent the presence of the crystalline phase of SnO_2 (the tetragonal SnO_2 cassiterite).
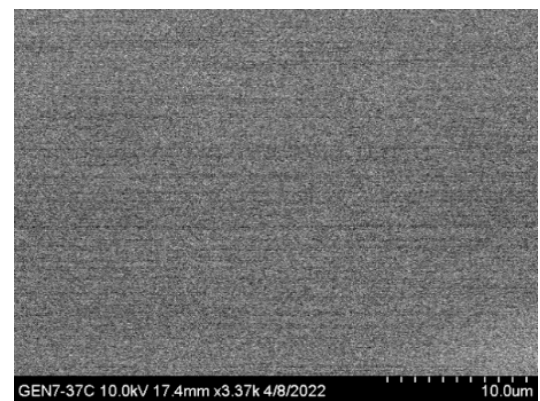

Figure 8. SEM image of the surface of In-doped SnO_2 thin film.

Figure 9. EDS spectrum of the as-deposited In-doped SnO_2 film.

3.2. Humidity Sensing Performance

The humidity sensing performance of the In-doped SnO_2 sensing film was investigated in a wide range of relative humidity levels (15–90% RH) at an operating frequency of 35 kHz. The dynamic impedance response curve versus time with increasing relative humidity is shown in Figure 10. The impedance of the sensor returned to its baseline state as the sensor switched between the different relative humidity levels. At a specific % RH, the impedance of the film initially decreased due to the adsorption of water molecules; however, when exposed to N_2 gas, the desorption caused the impedance to return to its baseline state.
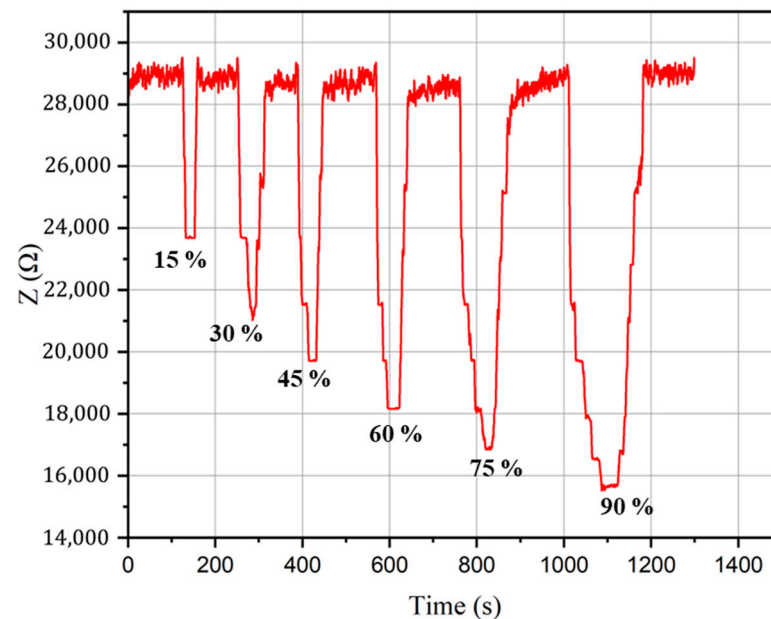
Figure 10. Dynamic impedance response curve versus time with gradually increasing % RH.

Figure 11 illustrates the variation in the impedance of In-doped SnO_2 as a function of the relative humidity level at room temperature. The fitting function of impedance (Z) and the relative humidity of the In-doped SnO_2 humidity sensor was $Z = (-0.13 \times RH + 24.6)$ kΩ with a regression coefficient R^2 of 0.980. As shown in the figure, the impedance decreased linearly with increasing relative humidity, but the sensor response increased with increasing relative humidity. This result demonstrated the excellent linearity of the sensor response to RH, which is essential for practical applications. Furthermore, sensitivity (S) is also an important parameter in quantifying the performance of humidity sensors. It is defined in [46] as the variation in impedance for relative humidity and is mathematically expressed as

$$ S = \frac{\Delta Z}{\Delta \% RH} k\Omega/\%RH, \tag{1} $$

where ΔZ and $\Delta \% RH$ represent the change in impedance and relative humidity, respectively. The sensitivity value was 103.15 Ω/%RH in the range of 10 to 90% RH. In addition, response time, recovery time, repeatability, and hysteresis are significant indicators to evaluate humidity sensor performance [51,52].

To investigate the repeatability of the humidity sensor, the sensor was exposed to a level of 45% RH for five successive cycles. Figure 12 shows the impedance variations of the In-doped SnO_2 sensor in five cycles switching between N_2 gas and different relative humidity. As shown in the figure, at a relative humidity of 45%, the change in baseline and final impedance values was almost negligible after multiple cycles. Moreover, the standard deviation of the impedance value to 45% RH was calculated and found to be 0.002, indicating excellent dynamic stability and repeatability of the sensor. Response time (t_{res}) is defined as the time it takes for the impedance to reach 90% of its final value after exposure

to humid air, and recovery time (t_{rec}) is defined as the time it takes for the impedance to return 90% of its baseline value [56]. Based on the dynamic impedance-time curve in Figure 12, the response and recovery times of the In-doped SnO_2-based humidity sensor were estimated to be 10 and 21 s, respectively.
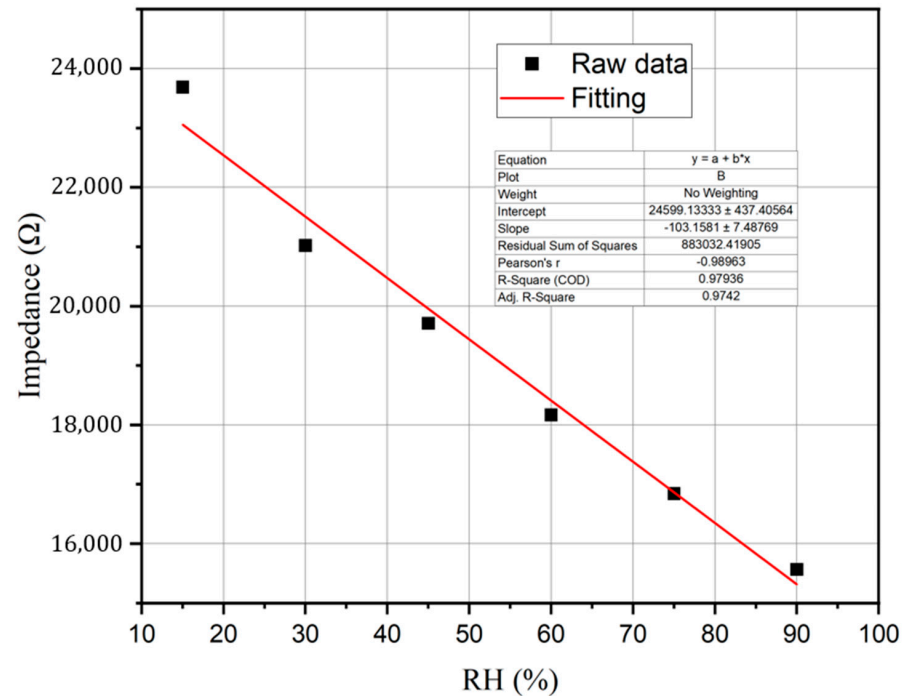
Figure 11. Impedance vs. %RH for In-doped SnO_2 humidity sensor with the trend line.
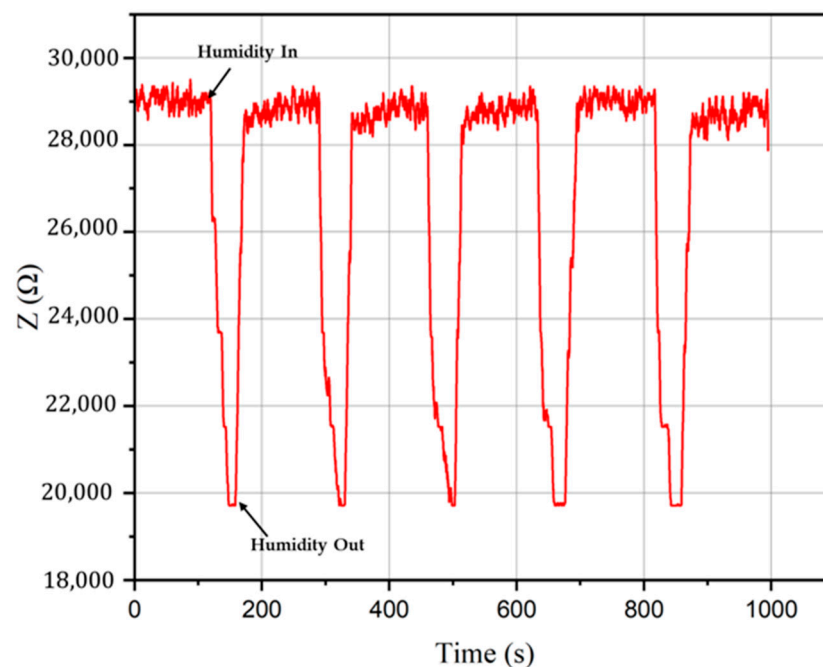
Figure 12. Dynamic impedance measurements for determining the response and recovery times of the humidity sensor.

To study the hysteresis characteristic of the sensor, the sensor was consecutively exposed to different levels of relative humidity (adsorption process) and then followed by a downward one (desorption process). Figure 13 shows the sensor hysteresis during adsorp-
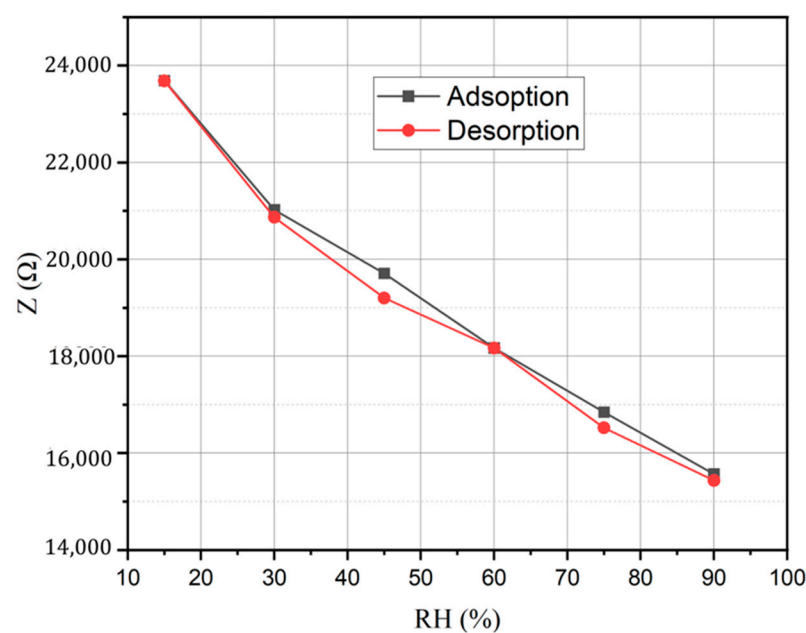
tion and desorption. In the adsorption process, the impedance decreased as the relative humidity increased. However, in the desorption process, the impedance increased as the relative humidity decreased. Hysteresis was calculated by measuring the impedance difference between the adsorption and desorption measurements at a particular RH value and then divided by the full output range [57], mathematically expressed as $H = \Delta H_{max}/2F_{FS}$, where ΔH_{max} and F_{FS} are the maximum hysteresis value and the full-scale output, respectively. The hysteresis of the sensor was about 2.58%, further demonstrating the reversibility of the sensor.

Finally, the long-term stability of the In-doped SnO_2-based humidity sensor was investigated by exposing it to humid air (45% RH) for one month. Figure 14 shows the variation in the impedance of the humidity sensor to 45% RH as a function of time during that period. The variation in impedance was less than 2%, suggesting that the long-term stability of the sensor is suitable for use in practical applications.

Table 1 compares the humidity sensing performance of the In-doped SnO_2-based humidity sensor used in this study with other previously reported SnO_2-based humidity sensors. Compared to others, the In-doped SnO_2-based humidity sensor exhibited fast response and recovery times. In general, the In-doped SnO_2-based sensor has great potential in practical humidity sensing applications.

Table 1. Comparison of humidity sensors based on SnO_2 from this and previously reported work.

| Sensing Material	t_{res} (s)	t_{rec} (s)	Ref.
Co-doped SnO_2/rGO	522	100	[58]
rGO/SnO_2	6–102	6–9	[59]
rGO-SnO_2	10	60	[60]
ZnO/SnO_2	411	98	[61]
Sb-doped SnO_2	40	64	[62]
Ni-doped SnO_2	15	4	[49]
MoS_2/SnO_2	17	6	[47]
WS_2/SnO_2	100	100	[57]
In-doped SnO_2	10	21	This work

Figure 13. Plot of the impedance vs. relative humidity for the adsorption and desorption cycles showing hysteresis characteristics.
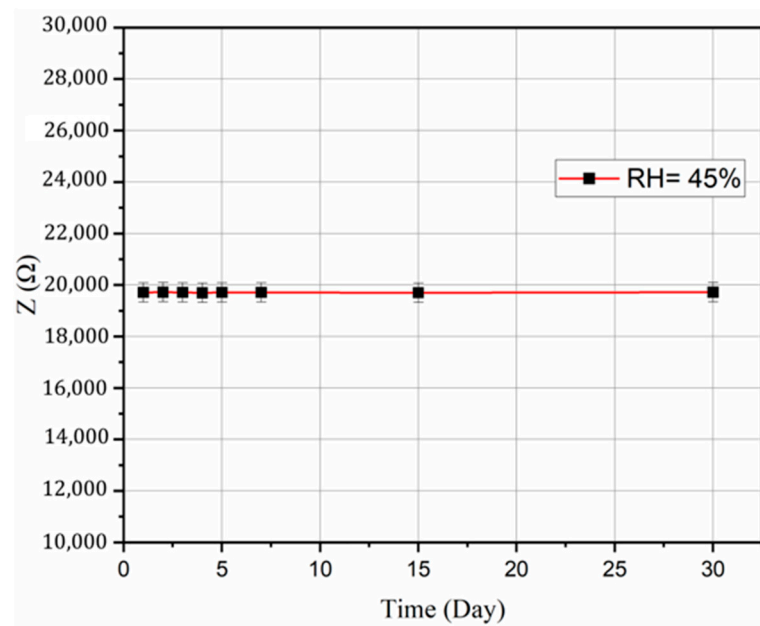
Figure 14. Long-term stability of the humidity sensor measured for 30 days.

3.3. Humidity Sensing Mechanism

The humidity sensing mechanism of the sensor was associated with the adsorption of water molecules on the surface of the In-doped SnO_2 film, which caused a change in the electrical properties of the sensing film. Figure 15 shows the schematic diagram of the adsorption process of water molecules on the surface of In-doped SnO_2, which resulted in the formation of chemisorbed and physisorbed layers. Briefly, at low RH levels, upon exposure to humid air, water molecules decomposed into protons (H^+) and hydroxide ions (OH^-) as a result of self-ionization and surface collision with the film surface [63,64]. Subsequently, OH^- interacted with cations on the surface of In-doped SnO_2 and formed a chemisorption layer. This phenomenon caused a decrease in the potential barrier and the disappearance of the depletion layer by reducing the electron affinity of the cations and removing the electrons captured in a dry environment [62–64]. In turn, the bulk conductivity and the dielectric constant increased. Therefore, the sensor was quite sensitive, even at low RH levels. However, at low humidity, only a small amount of water was absorbed, leading to the appearance of a discontinuous water layer on the film surface [65]. It makes the conduction of protons to neighboring OH^- ions challenging. Therefore, electron conduction was more dominant than ion conduction.
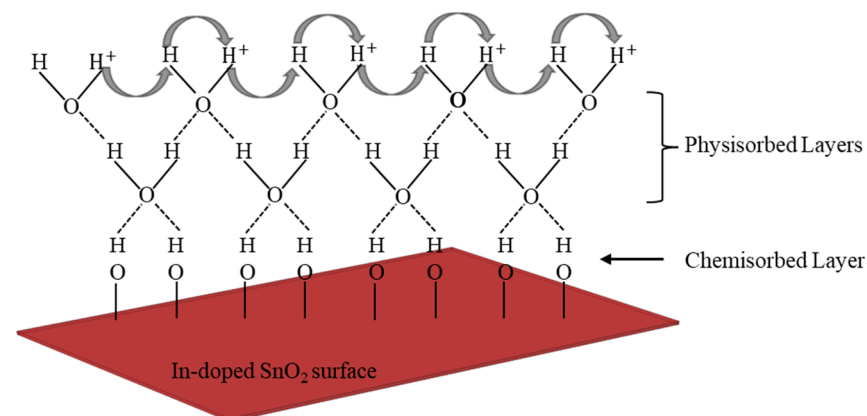
Figure 15. The humidity sensing mechanism of In-doped SnO_2 thin film.

In mid-RH, as the humidity increased, the adsorption of water molecules also increased. The adsorption of more water molecules led to the formation of a physisorbed layer on the surface of the film through hydrogen bonds [47]. Water molecules dissociated and produced hydronium ions (H_3O^+) under a strong electrostatic field in the chemisorption layer [66]. Subsequently, H_3O^+ was converted back to H_2O, and more protons were released as a result of the applied electric fields, acting as a source of protons. Due to the formation of additional layers, protons (H^+) can move to adjacent water molecules [67]. As a result, ionic conduction becomes effective, and the impedance decreases further. In addition, as more and more water molecules were absorbed, subsequent physisorbed layers gradually formed. At high RH, as the humidity increases further, a large volume of water molecules could be absorbed, creating a continuous water layer. This layer accelerated the free movement of protons toward adjacent water molecules. This leads to the formation of a constant dipole and electrolyte layer between the electrodes. As a result, the dielectric constant and bulk conductivity increased further [68]. The porous structure of In-doped SnO_2 can also play a substantial role in facilitating the absorption of water molecules and, in turn, improving the sensor's performance.

4. Conclusions

In summary, we demonstrated the controllable synthesis of large-area and thickness-tunable $NbTe_2$ nanosheets by optimizing the deposition parameters during the PLD process. The X-ray diffraction pattern exhibited the pure $NbTe_2$ phase. The stoichiometric composition of the $NbTe_2$ film was confirmed using EDS. The PLD process was also used for the direct synthesis of the In-doped SnO_2 sensing film on the substrate. The X-ray diffraction pattern showed the crystal structure of In-doped SnO_2. Besides, the SEM image revealed the presence of nanopores on the surface of the film. An impedimetric humidity sensor based on In-doped SnO_2 (8:92 wt%) was developed, and its sensing response was investigated in a wide range of relative humidity (15–90% RH) at room temperature. The In-doped SnO_2 humidity sensor showed a superb linear response, low hysteresis, long-term stability, a remarkable sensitivity of 103.15 Ω/%RH, and a short response and recovery times of 10 and 21 s, respectively. In addition, the sensor had good repeatability. Finally, the humidity sensing mechanism of In-doped SnO_2 was discussed in detail. Overall, the results highlighted that In-doped SnO_2 has a good prospect as a sensing material for practical humidity sensing applications. Additionally, $NbTe_2$ is a promising electrode material that can serve as a building block for the construction of electronic devices.

References

1. Bhimanapati, G.R.; Lin, Z.; Meunier, V.; Jung, Y.; Cha, J.; Das, S.; Xiao, D.; Son, Y.; Strano, M.S.; Cooper, V.R. Recent advances in two-dimensional materials beyond graphene. *ACS Nano* **2015**, *9*, 11509–11539. [CrossRef] [PubMed]
2. Bernardi, M.; Palummo, M.; Grossman, J.C. Extraordinary sunlight absorption and one nanometer thick photovoltaics using two-dimensional monolayer materials. *Nano Lett.* **2013**, *13*, 3664–3670. [CrossRef] [PubMed]
3. Cheng, R.; Jiang, S.; Chen, Y.; Liu, Y.; Weiss, N.; Cheng, H.-C.; Wu, H.; Huang, Y.; Duan, X. Few-layer molybdenum disulfide transistors and circuits for high-speed flexible electronics. *Nat. Commun.* **2014**, *5*, 5143. [CrossRef] [PubMed]

4.	Chen, X.; Liu, X.; Wu, B.; Nan, H.; Guo, H.; Ni, Z.; Wang, F.; Wang, X.; Shi, Y.; Wang, X. Improving the performance of graphene phototransistors using a heterostructure as the light-absorbing layer. *Nano Lett.* **2017**, *17*, 6391–6396. [CrossRef] [PubMed]

5.	Xu, X.; Yao, W.; Xiao, D.; Heinz, T.F. Spin and pseudospins in layered transition metal dichalcogenides. *Nat. Phys.* **2014**, *10*, 343–350. [CrossRef]

6.	Wang, S.-W.; Medina, H.; Hong, K.-B.; Wu, C.-C.; Qu, Y.; Manikandan, A.; Su, T.-Y.; Lee, P.-T.; Huang, Z.-Q.; Wang, Z. Thermally strained band gap engineering of transition-metal dichalcogenide bilayers with enhanced light–matter interaction toward excellent photodetectors. *ACS Nano* **2017**, *11*, 8768–8776. [CrossRef] [PubMed]

7.	Walter, T.N.; Lee, S.; Zhang, X.; Chubarov, M.; Redwing, J.M.; Jackson, T.N.; Mohney, S.E. Atomic layer deposition of ZnO on MoS$_2$ and WSe$_2$. *Appl. Surf. Sci.* **2019**, *480*, 43–51. [CrossRef]

8.	Koperski, M.; Molas, M.R.; Arora, A.; Nogajewski, K.; Slobodeniuk, A.O.; Faugeras, C.; Potemski, M. Optical properties of atomically thin transition metal dichalcogenides: Observations and puzzles. *Nanophotonics* **2017**, *6*, 1289–1308. [CrossRef]

9.	Taniguchi, K.; Matsumoto, A.; Shimotani, H.; Takagi, H. Electric-field-induced superconductivity at 9.4 K in a layered transition metal disulphide MoS$_2$. *Appl. Phys. Lett.* **2012**, *101*, 042603. [CrossRef]

10.	Song, X.; Hu, J.; Zeng, H. Two-dimensional semiconductors: Recent progress and future perspectives. *J. Mater. Chem. C* **2013**, *1*, 2952–2969. [CrossRef]

11.	Wang, Q.H.; Kalantar-Zadeh, K.; Kis, A.; Coleman, J.N.; Strano, M.S. Electronics and optoelectronics of two-dimensional transition metal dichalcogenides. *Nat. Nanotechnol.* **2012**, *7*, 699–712. [CrossRef] [PubMed]

12.	Meng, L.; Zhou, Z.; Xu, M.; Yang, S.; Si, K.; Liu, L.; Wang, X.; Jiang, H.; Li, B.; Qin, P. Anomalous thickness dependence of Curie temperature in air-stable two-dimensional ferromagnetic 1T-CrTe$_2$ grown by chemical vapor deposition. *Nat. Commun.* **2021**, *12*, 809. [CrossRef]

13.	Sipos, B.; Kusmartseva, A.F.; Akrap, A.; Berger, H.; Forró, L.; Tutiš, E. From Mott state to superconductivity in 1T-TaS$_2$. *Nat. Mater.* **2008**, *7*, 960–965. [CrossRef] [PubMed]

14.	Wilson, J.A.; Di Salvo, F.; Mahajan, S. Charge-density waves and superlattices in the metallic layered transition metal dichalcogenides. *Adv. Phys.* **1975**, *24*, 117–201. [CrossRef]

15.	Zhang, Z.; Niu, J.; Yang, P.; Gong, Y.; Ji, Q.; Shi, J.; Fang, Q.; Jiang, S.; Li, H.; Zhou, X. Van der Waals epitaxial growth of 2D metallic vanadium diselenide single crystals and their extra-high electrical conductivity. *Adv. Mater.* **2017**, *29*, 1702359. [CrossRef] [PubMed]

16.	Joe, Y.I.; Chen, X.; Ghaemi, P.; Finkelstein, K.; de La Peña, G.; Gan, Y.; Lee, J.; Yuan, S.; Geck, J.; MacDougall, G. Emergence of charge density wave domain walls above the superconducting dome in 1T-TiSe$_2$. *Nat. Phys.* **2014**, *10*, 421–425. [CrossRef]

17.	Shi, J.; Huan, Y.; Zhao, X.; Yang, P.; Hong, M.; Xie, C.; Pennycook, S.; Zhang, Y. Two-dimensional metallic vanadium ditelluride as a high-performance electrode material. *ACS Nano* **2021**, *15*, 1858–1868. [CrossRef] [PubMed]

18.	Shi, J.; Wang, X.; Zhang, S.; Xiao, L.; Huan, Y.; Gong, Y.; Zhang, Z.; Li, Y.; Zhou, X.; Hong, M. Two-dimensional metallic tantalum disulfide as a hydrogen evolution catalyst. *Nat. Commun.* **2017**, *8*, 958. [CrossRef]

19.	Feng, J.; Peng, L.; Wu, C.; Sun, X.; Hu, S.; Lin, C.; Dai, J.; Yang, J.; Xie, Y. Giant moisture responsiveness of VS2 ultrathin nanosheets for novel touchless positioning interface. *Adv. Mater.* **2012**, *24*, 1969–1974. [CrossRef]

20.	Feng, J.; Sun, X.; Wu, C.; Peng, L.; Lin, C.; Hu, S.; Yang, J.; Xie, Y. Metallic few-layered VS2 ultrathin nanosheets: High two-dimensional conductivity for in-plane supercapacitors. *J. Am. Chem. Soc.* **2011**, *133*, 17832–17838. [CrossRef]

21.	GUZMA'N, R.; Lavela, P.; Morales, J.; Tirado, J. VSe2-ySy electrodes in lithium and lithium-ion cells. *J. Appl. Electrochem.* **1997**, *27*, 1207–1211. [CrossRef]

22.	Gopalakrishnan, D.; Lee, A.; Thangavel, N.K.; Arava, L.M.R. Facile synthesis of electrocatalytically active NbS$_2$ nanoflakes for an enhanced hydrogen evolution reaction (HER). *Sustain. Energy Fuels* **2018**, *2*, 96–102. [CrossRef]

23.	Wang, X.; He, J.; Zhou, B.; Zhang, Y.; Wu, J.; Hu, R.; Liu, L.; Song, J.; Qu, J. Bandgap-tunable preparation of smooth and large two-dimensional antimonene. *Angew. Chem.* **2018**, *130*, 8804–8809. [CrossRef]

24.	Al-Dulaimi, N.; Lewis, E.A.; Lewis, D.J.; Howell, S.K.; Haigh, S.J.; O'Brien, P. Sequential bottom-up and top-down processing for the synthesis of transition metal dichalcogenide nanosheets: The case of rhenium disulfide (ReS$_2$). *Chem. Commun.* **2016**, *52*, 7878–7881. [CrossRef] [PubMed]

25.	Coleman, J.N.; Lotya, M.; O'Neill, A.; Bergin, S.D.; King, P.J.; Khan, U.; Young, K.; Gaucher, A.; De, S.; Smith, R.J. Two-dimensional nanosheets produced by liquid exfoliation of layered materials. *Science* **2011**, *331*, 568–571. [CrossRef] [PubMed]

26.	Zhao, S.; Hotta, T.; Koretsune, T.; Watanabe, K.; Taniguchi, T.; Sugawara, K.; Takahashi, T.; Shinohara, H.; Kitaura, R. Two-dimensional metallic NbS2: Growth, optical identification and transport properties. *2D Mater.* **2016**, *3*, 025027. [CrossRef]

27.	Ji, Q.; Li, C.; Wang, J.; Niu, J.; Gong, Y.; Zhang, Z.; Fang, Q.; Zhang, Y.; Shi, J.; Liao, L. Metallic vanadium disulfide nanosheets as a platform material for multifunctional electrode applications. *Nano Lett.* **2017**, *17*, 4908–4916. [CrossRef]

28.	Ji, Q.; Zhang, Y.; Zhang, Y.; Liu, Z. Chemical vapour deposition of group-VIB metal dichalcogenide monolayers: Engineered substrates from amorphous to single crystalline. *Chem. Soc. Rev.* **2015**, *44*, 2587–2602. [CrossRef]

29.	Govind Rajan, A.; Warner, J.H.; Blankschtein, D.; Strano, M.S. Generalized mechanistic model for the chemical vapor deposition of 2D transition metal dichalcogenide monolayers. *ACS Nano* **2016**, *10*, 4330–4344. [CrossRef]

30.	Park, H.; Mun, J.; Joung, D.; Wie, J.J.; Jeong, S.-H.; Kang, S.-W. A photolithographic method for fabricating electron devices based on MOCVD-grown MoS$_2$. *Chem. Eng. J.* **2020**, *382*, 122944. [CrossRef]

31. Lin, Z.; McCreary, A.; Briggs, N.; Subramanian, S.; Zhang, K.; Sun, Y.; Li, X.; Borys, N.J.; Yuan, H.; Fullerton-Shirey, S.K. 2D materials advances: From large scale synthesis and controlled heterostructures to improved characterization techniques, defects and applications. *2D Mater.* **2016**, *3*, 042001. [CrossRef]

32. Park, S.; Park, J.; Kim, Y.; Bae, S.; Kim, T.-W.; Park, K.-I.; Hong, B.H.; Jeong, C.K.; Lee, S.-K. Laser-directed synthesis of strain-induced crumpled MoS_2 structure for enhanced triboelectrification toward haptic sensors. *Nano Energy* **2020**, *78*, 105266. [CrossRef]

33. Serrao, C.R.; Diamond, A.M.; Hsu, S.-L.; You, L.; Gadgil, S.; Clarkson, J.; Carraro, C.; Maboudian, R.; Hu, C.; Salahuddin, S. Highly crystalline MoS_2 thin films grown by pulsed laser deposition. *Appl. Phys. Lett.* **2015**, *106*, 052101. [CrossRef]

34. Loh, T.A.; Chua, D.H. Growth mechanism of pulsed laser fabricated few-layer MoS2 on metal substrates. *ACS Appl. Mater. Interfaces* **2014**, *6*, 15966–15971. [CrossRef]

35. Siegel, G.; Venkata Subbaiah, Y.; Prestgard, M.C.; Tiwari, A. Growth of centimeter-scale atomically thin MoS_2 films by pulsed laser deposition. *APL Mater.* **2015**, *3*, 056103. [CrossRef]

36. Grangeon, F.; Sassoli, H.; Mathey, Y.; Autric, M.; Pailharey, D.; Marine, W. Pulsed laser deposition of NbTex thin films. *Appl. Surf. Sci.* **1995**, *86*, 160–164. [CrossRef]

37. Hamouche, H.; Makhlouf, S.; Chaouchi, A.; Laghrouche, M. Humidity sensor based on keratin bio polymer film. *Sens. Actuators A Phys.* **2018**, *282*, 132–141. [CrossRef]

38. Ismail, A.; Mamat, M.; Yusoff, M.; Malek, M.; Zoolfakar, A.; Rani, R.; Suriani, A.; Mohamed, A.; Ahmad, M.; Rusop, M. Enhanced humidity sensing performance using Sn-Doped ZnO nanorod Array/SnO_2 nanowire heteronetwork fabricated via two-step solution immersion. *Mater. Lett.* **2018**, *210*, 258–262. [CrossRef]

39. Li, P.; Zheng, X.; Zhang, Y.; Yuan, M.; Jiang, B.; Deng, S. Humidity sensor based on electrospun $(Na_{0.5}Bi_{0.5})_{0.94}$ TiO_3–$Ba_{0.06}TiO_3$ nanofibers. *Ceram. Int.* **2015**, *41*, 14251–14257. [CrossRef]

40. Jeong, H.; Noh, Y.; Lee, D. Highly stable and sensitive resistive flexible humidity sensors by means of roll-to-roll printed electrodes and flower-like TiO_2 nanostructures. *Ceram. Int.* **2019**, *45*, 985–992. [CrossRef]

41. Park, S.; Lee, D.; Kwak, B.; Lee, H.-S.; Lee, S.; Yoo, B. Synthesis of self-bridged ZnO nanowires and their humidity sensing properties. *Sens. Actuators B Chem.* **2018**, *268*, 293–298. [CrossRef]

42. Kim, H.; Park, S.; Park, Y.; Choi, D.; Yoo, B.; Lee, C.S. Fabrication of a semi-transparent flexible humidity sensor using kinetically sprayed cupric oxide film. *Sens. Actuators B Chem.* **2018**, *274*, 331–337. [CrossRef]

43. Musa, M.; Mamat, M.; Vasimalai, N.; Banu, I.S.; Malek, M.; Ahmad, M.; Suriani, A.; Mohamed, A.; Rusop, M. Fabrication and structural properties of flower-like TiO_2 nanorod array films grown on glass substrate without FTO layer. *Mater. Lett.* **2020**, *273*, 127902. [CrossRef]

44. Parimon, N.; Mamat, M.; Banu, I.S.; Vasimalai, N.; Ahmad, M.; Suriani, A.; Mohamed, A.; Rusop, M. Annealing temperature dependency of structural, optical and electrical characteristics of manganese-doped nickel oxide nanosheet array films for humidity sensing applications. *Nanomater. Nanotechnol.* **2021**, *11*, 1847980420982788. [CrossRef]

45. Toloman, D.; Popa, A.; Stan, M.; Socaci, C.; Biris, A.; Katona, G.; Tudorache, F.; Petrila, I.; Iacomi, F. Reduced graphene oxide decorated with Fe doped SnO_2 nanoparticles for humidity sensor. *Appl. Surf. Sci.* **2017**, *402*, 410–417. [CrossRef]

46. Zhang, D.; Sun, Y.; Li, P.; Zhang, Y. Facile fabrication of MoS_2-modified SnO_2 hybrid nanocomposite for ultrasensitive humidity sensing. *ACS Appl. Mater. Interfaces* **2016**, *8*, 14142–14149. [CrossRef] [PubMed]

47. Zhao, Y.; Yang, B.; Liu, J. Effect of interdigital electrode gap on the performance of SnO_2-modified MoS_2 capacitive humidity sensor. *Sens. Actuators B Chem.* **2018**, *271*, 256–263. [CrossRef]

48. Li, F.; Li, P.; Zhang, H. Preparation and research of a high-performance ZnO/SnO_2 humidity sensor. *Sensors* **2022**, *22*, 293. [CrossRef]

49. Modak, M.; Choudhari, U.; Mahajan, S.; Hambir, S.; Jagtap, S. *Studies on Ni–SnO_2 Nanocomposites for Humidity Sensing Application*; Wiley Online Library: New York, NY, USA, 2022; Volume 401, p. 2100370.

50. Dwiputra, M.A.; Fadhila, F.; Imawan, C.; Fauzia, V. The enhanced performance of capacitive-type humidity sensors based on ZnO nanorods/WS2 nanosheets heterostructure. *Sens. Actuators B Chem.* **2020**, *310*, 127810. [CrossRef]

51. Caglar, M.; Atar, K.C. Effect of both deposition temperature and indium doping on the properties of sol–gel dip–coated SnO_2 films. *Spectrochim. Acta Part A Mol. Biomol. Spectrosc.* **2012**, *96*, 882–888. [CrossRef]

52. Sujatha Lekshmy, S.; Joy, K. Structural and optoelectronic properties of indium doped SnO_2 thin films deposited by sol gel technique. *J. Mater. Sci. Mater. Electron.* **2014**, *25*, 1664–1672. [CrossRef]

53. Teldja, B.; Noureddine, B.; Azzeddine, B.; Meriem, T. Effect of indium doping on the UV photoluminescence emission, structural, electrical and optical properties of spin-coating deposited SnO_2 thin films. *Optik* **2020**, *209*, 164586. [CrossRef]

54. Bhatia, G.; Acharya, A.D.; Patidar, M.; Gupta, V.; Shrivastava, S.; Ganesan, V. Tuning of structural, morphological, optical and electrical properties of SnO_2 by indium inclusion. *Bull. Mater. Sci.* **2021**, *44*, 187. [CrossRef]

55. Alemayehu, B.D. Development and Characterization of Multi-Sensor Platforms for Real-Time Sensing Applications. Ph.D. Thesis, University of Dayton, Dayton, OH, USA, 2023.

56. Shah, Z.; Shaheen, K.; Arshad, T.; Ahmad, B.; Khan, S.B.; Suo, H. Al doped Sr and Cd metal oxide nanomaterials for resistive response of humidity sensing. *Mater. Chem. Phys.* **2022**, *290*, 126632. [CrossRef]

57. Zhang, D.; Cao, Y.; Li, P.; Wu, J.; Zong, X. Humidity-sensing performance of layer-by-layer self-assembled tungsten disulfide/tin dioxide nanocomposite. *Sens. Actuators B Chem.* **2018**, *265*, 529–538. [CrossRef]

58. Madbouly, A.I.; Morsy, M.; Alnahdi, R.F. Microwave-assisted synthesis of Co-doped SnO_2/rGO for indoor humidity monitoring. *Ceram. Int.* **2022**, *48*, 13604–13614. [CrossRef]
59. Zhang, D.; Chang, H.; Li, P.; Liu, R.; Xue, Q. Fabrication and characterization of an ultrasensitive humidity sensor based on metal oxide/graphene hybrid nanocomposite. *Sens. Actuators B Chem.* **2016**, *225*, 233–240. [CrossRef]
60. Karthick, S.; Lee, H.-S.; Kwon, S.-J.; Natarajan, R.; Saraswathy, V. Standardization, calibration, and evaluation of tantalum-nano rGO-SnO_2 composite as a possible candidate material in humidity sensors. *Sensors* **2016**, *16*, 2079. [CrossRef]
61. Md Sin, N.; Mamat, M.; Malek, M.; Rusop, M. Fabrication of nanocubic ZnO/SnO_2 film-based humidity sensor with high sensitivity by ultrasonic-assisted solution growth method at different Zn: Sn precursor ratios. *Appl. Nanosci.* **2014**, *4*, 829–838. [CrossRef]
62. Panday, M.; Upadhyay, G.K.; Purohit, L. Sb incorporated SnO_2 nanostructured thin films for CO_2 gas sensing and humidity sensing applications. *J. Alloys Compd.* **2022**, *904*, 164053. [CrossRef]
63. Jyothilal, H.; Shukla, G.; Walia, S.; Kundu, S.; Angappane, S. Humidity sensing and breath analyzing applications of TiO_2 slanted nanorod arrays. *Sens. Actuators A Phys.* **2020**, *301*, 111758. [CrossRef]
64. Kumar, V.; Chauhan, V.; Ram, J.; Gupta, R.; Kumar, S.; Chaudhary, P.; Yadav, B.; Ojha, S.; Sulania, I.; Kumar, R. Study of humidity sensing properties and ion beam induced modifications in SnO_2-TiO_2 nanocomposite thin films. *Surf. Coat. Technol.* **2020**, *392*, 125768. [CrossRef]
65. Li, X.; Feng, W.; Zhang, X.; Lin, S.; Chen, Y.; Chen, C.; Chen, S.; Wang, W.; Zhang, Y. Facile fabrication of laser-scribed-graphene humidity sensors by a commercial DVD drive. *Sens. Actuators B Chem.* **2020**, *321*, 128483. [CrossRef]
66. Guo, L.; Li, X.; Li, W.; Gou, C.; Zheng, M.; Zhang, Y.; Chen, Z.; Hong, Y. High-sensitive humidity sensor based on MoS_2/graphene oxide quantum dot nanocomposite. *Mater. Chem. Phys.* **2022**, *287*, 126146. [CrossRef]
67. Agmon, N. The grotthuss mechanism. *Chem. Phys. Lett.* **1995**, *244*, 456–462. [CrossRef]
68. Zhang, H.; Yu, S. Impedance humidity sensors based on metal oxide semiconductors: Characteristics and mechanism. In *Modeling, Characterization, and Production of Nanomaterials*; Elsevier: Amsterdam, The Netherlands, 2023; pp. 549–580.